Computational Particle Mechanics (2025) 12:2081–2100
https://doi.org/10.1007/s40571-025-00906-3

DEM analysis of friction of cylindrical pinewood pellets with corrugated steel silo walls

Eutiquio Gallego[1] · **Marcos Madrid**[2] · **José María Fuentes**[1] · **Joanna Wiącek**[3] · **Ana Grande**[1] · **Francisco Ayuga**[1]

Received: 18 September 2024 / Revised: 13 December 2024 / Accepted: 2 January 2025 / Published online: 8 March 2025

Abstract

Steel silos with corrugated walls exhibit friction phenomena between the bulk material and the silo wall quite different from those produced in smooth walls. A silo model was designed, and discrete element method (DEM) simulations were performed to analyze an influence of the depth and wavelengths of corrugations on mass flow rate, wall pressures, location of the shear band and effective wall friction coefficient. The dimensions of the geometry adopted correspond to one of the vertical sections of the silo model with corrugated steel walls instrumented by the authors. This silo model consisted of a square cross section (0.45 x 0.45 m^2) and 0.75 m in height, a flat bottom with a centric, square outlet (0.06 x 0.06 m^2), corrugated lateral steel walls, and smooth, transparent methacrylate front and back walls. The bulk material was pinewood pellets, whose mechanical and numerical properties had been previously obtained by the authors. The numerical results show an influence of the depth of corrugation and the wavelength on the velocity of the granular particles and the friction forces against the wall. The initial position of the shear band was found to be placed between 1 and 3.5 times the average size of the particles from the vertical line connecting two consecutive corrugation peaks closest to the silo outlet. The effective wall friction coefficient for corrugated walls depends on the wavelength and the depth of the corrugations, varying in the range of 0.42 to 0.9, in opposition to the single theoretical value of 0.78 proposed by Eurocode EN 1991-4, for a sinusoidal profile, regardless of the geometrical parameters.

Keywords Friction · silo · corrugated wall · DEM · shear band

List of symbols

L	Side length of the square cross section of the silo (m)
H_T	Height of the experimental silo (m)
H	Height above silo outlet (m)
M	Mass of the bulk material stored in the silo (kg)
W	Weight of the bulk material stored in the silo (N)
T	Time (s)
R_n	Relative roughness of the corrugated wall
μ_{eff}	Effective wall friction coefficient
μ_w	Friction coefficient against a smooth wall
a_w	Wall contact factor
ϕ_i	Angle of internal friction of the bulk material (°)
ϕ_r	Angle of repose of the bulk material (°)
h_c	Corrugation depth (mm)

This research was funded by the Spanish "Agencia Estatal de Investigación" through the research project "Study of the structural behavior of corrugated wall silos using Discrete Element Models (SILODEM)", grant number PID2019-107051GBI00/AEI/10.13039/501100011033".

✉ Eutiquio Gallego
eutiquio.gallego@upm.es

Marcos Madrid
marcosmadrid@googlemail.com

José María Fuentes
jm.fuentes@upm.es

Joanna Wiącek
j.wiacek@ipan.lublin.pl

Ana Grande
ana.grandeguti@upm.es

Francisco Ayuga
francisco.ayuga@upm.es

[1] BIPREE Research Group, ETSI Agronomica Alimentaria y de Biosistemas, Universidad Politecnica de Madrid, 28040 Madrid, Spain

[2] IFLYSIB-CONICET and UTN-FRLP, 1900 La Plata, Argentina

[3] Institute of Agrophysics, Polish Academy of Sciences, Doświadczalna 4, 20-290 Lublin, Poland

l	Corrugation wavelength (mm)
d_{50}	Mean equivalent diameter of particles (mm)
L_p	Length of pinewood particles (mm)
v	Mean particle velocity (mm/s)
Q	Mass flow rate (kg/s)
x_c	Lateral distance to silo center (mm)
x_w	Lateral distance to silo wall (mm)
τ	Shear stress (Pa)
F_w	Wall frictional forces (N)
F_v	Vertical forces over silo bottom (N)
p_h	Wall lateral pressures (Pa)
p_w	Wall frictional pressures (Pa)
σ	Standard deviation
CV	Coefficient of variance
ρ	Density (kg/m^3)
ν	Coefficient of Poisson
E	Modulus of elasticity of bulk material (N/mm^2)
E_i	Modulus of elasticity of particle i (N/mm^2)
E^*	Equivalent modulus of elasticity
G	Shear modulus of elasticity of bulk material (N/mm^2)
G_i	Shear modulus of elasticity of particle i (N/mm^2)
G^*	Equivalent shear modulus of elasticity
e_{pp}	Particle-to-particle coefficient of restitution
e_{pw}	Particle-to-wall coefficient of restitution
μ_{sp}	Particle-to-particle coefficient of static friction
μ_{sw}	Particle-to-wall coefficient of static friction
μ_{rp}	Particle-to-particle coefficient of rolling friction
μ_{rw}	Particle-to-wall coefficient of rolling friction
$\mathbf{F}_i^n$	Contact normal force in a specific instant of time
$(\mathbf{F}_i^n)_S$	Elastic spring component of the contact normal force
$(\mathbf{F}_i^n)_D$	Damping component of the contact normal force
$\mathbf{F}_i^t$	Contact tangential force in a specific instant of time
$(\mathbf{F}_i^t)_S$	Elastic spring component of the contact tangential force
$(\mathbf{F}_i^t)_D$	Damping component of the contact tangential force
K^n	Elastic constant of the contact normal force
C^n	Damping constant of the contact normal force
S_n	Elastic constant of the contact normal force
C^t	Damping constant of the contact tangential force
S^t	Elastic constant of the contact tangential force
$\delta_n \mathbf{n}_i$	Normal overlap (mm)
$\delta_t \mathbf{n}_i$	Tangential overlap (mm)
$\mathbf{V}_i^n$	Normal relative velocity (mm/s)
$\mathbf{V}_i^t$	Tangential relative velocity (mm/s)
R^*	Equivalent radius of particles (mm)
R_i	Radius of particle I (mm)
m_i	Mass of particle i (g)
m^*	Equivalent mass of particles in contact (g)
β	Critical damping coefficient

1 Introduction

Granular materials are used worldwide in many industries, e.g., chemical, pharmaceutical, agricultural, fuel or food, with over 45 billion tons of products being handled worldwide every year. Granular materials are usually stored in bins, hoppers, and silos, and they experience significant and particular structural and flow problems [2]. The appearance of friction forces is one of the main distinctive characteristics of the interaction between the bulk granular materials and the silo wall [19].

Steel silos with corrugated walls are widely used due to a more economical steel consumption and smaller weight, compared to the smooth wall solution [21]. However, corrugations affect the friction between the stored material and the wall, resulting in changes in the pressures exerted over the silo walls, the material flow inside the silo or the shear band formation [23, 44, 56]. These circumstances are not entirely considered by European standard EN 1991-4 used for silo design [6, 16, 50].

Few experimental works have been performed in metal silos with corrugated walls [44, 48]. Moore et al. [45] found that the value of the coefficient of friction measured for a corrugated steel surface was placed between two limiting values: the coefficient of friction for smooth walls (lower limit) and the coefficient of friction between grains (upper limit). Because of this, Zhang et al. [57] theorized that the existence of corrugations would imply that some particles would be trapped in the corrugation valleys without moving, while most of the bulk grain would be moving mainly following a vertical direction.

In consequence, friction between the moving grains and those trapped, and friction between grain and the wall may occur simultaneously. Eurocode standard [6] suggests the use of Eq. 1 to obtain the effective wall friction coefficient over a corrugated wall, μ_{eff}, thus considering both effects.

$$\mu_{eff} = (1 - a_w) \tan \phi_i + a_w \mu_w \tag{1}$$

where μ_w is the friction coefficient against a smooth wall, ϕ_i is the angle of internal friction of the bulk material and a_w is the wall contact factor. If a sinusoidal corrugated profile is used, then EN 1991-4 suggests to adopt a value of $a_w = 0.2$. The experimental works developed by Wiącek [54] with wheat grains reported significant differences with Wiacek regard to this proposed value. The works accomplished by several researchers [7, 40, 58] have shown that the inertial number [36, 43] is related to the effective wall friction coefficient over a corrugated wall through a power law [25].

The discrete element method (DEM) is a numerical technique that allows the particles and the container to be simultaneously represented. For this reason, it has been used

to study a great variety of silo problems and phenomena such as flow regimes [13, 59], stress distributions [26], segregation [10], clogging [5], residence time of particles [20] or discharge rate [17, 27, 60]. Because of this, DEM has also been widely used to understand the principles governing friction in granular systems, e.g., reproducing conventional shear tests [41, 51], identifying the location of shear bands [49], analyzing the effect of particle shape on the shear behavior of granular materials [1] or checking the degree of friction mobilization [37].

Nitka and Grabowski [22, 49] developed a DEM model to check the influence of the wall roughness on friction mechanisms when simulating a shear test with sand. Grabowski et al. [22] found that the relative roughness of the wall (defined as $R_n = h_c/d_{50}$, where h_c is the corrugation depth and d_{50} is the mean particle diameter) affects the friction effects observed. It was also found that the residual angle of internal friction and the width of the shear band increased up to a value of $R_n = 0.75$, but no significant changes were detected for larger values.

Grabowski et al. [23] developed a pseudo-3D DEM model to analyze shear location during quasi-static confined silo flow by also varying wall roughness and considering sand as the stored material. They found that wall roughness significantly affected the characteristics of internal shear zones. Kobyłka et al. [38] developed a DEM model where different annular segments were attached to the interior of the silo wall. These obstacles were found to cause significant changes, including flow modifications or changes in the shear forces applied over the walls.

Gallego et al. [19] developed a DEM model of a scale silo with corrugated steel walls with trapezoidal profile and filled with spherical glass beads to analyze the relationship between the frictional behavior of granular material and the geometry of the corrugations. The authors found that the ratio between the particle diameter and the corrugation depth influenced the material flow and friction forces. However, this model did not consider the influence of non-spherical shapes of particles, the distance between corrugations, the outlet width, or the filling method, among other factors.

The present work is focused on the analyses of the effects that the interaction between non-spherical particles of pinewood pellets with corrugated steel wall can produce on wall pressures, friction mechanism and flow for non-spherical particles, and considering different corrugation depths and wavelengths.

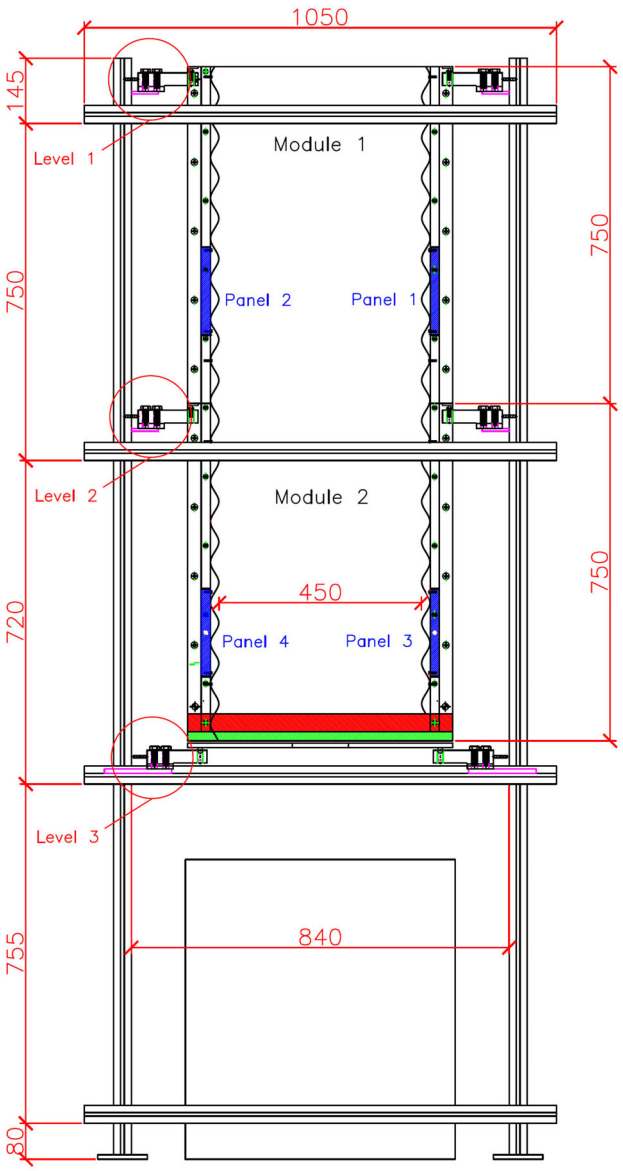

Fig. 1 Silo test model

2 Methodology

2.1 Experimental setup

The dimensions adopted for the DEM model match those of the experimental model silo implemented by the authors [16, 50]. The model silo was designed with a vertical body, a square cross section and a base that allowed for different discharge configurations (Fig. 1), but only a flat bottom was considered for DEM simulations in this work. The vertical body of the silo was composed of two independent modules, each 0.75 m in height and a cross section of $0.45 \times 0.45\ m^2$ one on top of the other with a 2 mm gap between them.

The outlet was placed in a central location with dimensions of $0.06 \times 0.06\, m^2$. The lateral walls of the silo were made of sinusoidal corrugated steel sheeting (wavelength $l = 0.075$ m, corrugation depth $h_c = 0.013$ m), fixed using countersunk screws onto a rigidity guaranteeing, deformation preventing DMF wood panel (thickness 20 mm).

The front and back walls were made of methacrylate, allowing the flow of material during discharge to be recorded. Besides, four test panels ($0.15 \times 0.15\, m^2$) were fitted to the lateral walls, two in the upper module and two in the lower module, with the center of each panel 0.25 m up from the bottom of each module.

The DEM model only considered one of the vertical modules due to the large computing resources required to simulate both modules. When the dimensions of real silo are compared with the mean diameter of tested particles ($d_{50} = 9.5mm$, see Sect. 2.2), the relative height (H_T/d_{50}) is 78.9, and relative width and length (L/d_{50}) are 47.4.

2.2 Numerical model

The discrete element method (DEM) introduced by Cundall and Strack [12] was used by employing EDEM software [14]. The Hertz–Mindlin contact theory of frictional elastic collisions [52] was considered for both particle-to-particle and particle-to-wall contacts, assuming viscous damping in the normal and tangential directions, and frictional damping in the tangential direction.

The contact normal force in a specific instant of time, $\mathbf{F}_i^n$, was composed of the elastic spring component, $(\mathbf{F}_i^n)_S$, and the damping component, $(\mathbf{F}_i^n)_D$ (Eq. 2). The elastic constant, K^n, and damping constant, C^n, can be calculated with Eqs. 3 and 4, where $\delta_n \mathbf{n}_i$ is the normal overlap and $\mathbf{V}_i^n$ is the normal relative velocity.

$$\mathbf{F}_i{}^n = (\mathbf{F}_i{}^n)_S + (\mathbf{F}_i{}^n)_D = K^n \delta_n \mathbf{n}_i + C^n (\mathbf{V}_i{}^n) \tag{2}$$

$$K^n = \frac{4}{3} E^* \sqrt{R^* \delta_n \mathbf{n}_i} \tag{3}$$

$$C^n = 2\sqrt{\frac{5}{6}} \beta \sqrt{m S_n} \tag{4}$$

$$E^* = \frac{E_i E_j}{E_i(1-\nu_j^2) + E_j(1-\nu_i^2)} \tag{5}$$

$$R^* = \frac{R_i R_j}{R_i + R_j} \tag{6}$$

$$\beta = \frac{-\ln e}{\sqrt{\ln e^2 + \pi^2}} \tag{7}$$

$$S_n = 2E^* \sqrt{R^* \delta_n \mathbf{n}_i} \tag{8}$$

$$m^* = \frac{m_i m_j}{m_i + m_j} \tag{9}$$

The elastic constant can be obtained from the equivalent Young's modulus, E^* (Eq. 5), and the equivalent radius, R^* (Eq. 6). The damping constant is calculated from the critical damping coefficient, β (Eq. 7), the normal stiffness, S_n (Eq. 8), and the equivalent mass, m^* (Eq. 9). The parameters obtained through Eqs. 5–9 consider the Young's modulus (E), Poisson's coefficient (ν), mass (m), and particle radius (R) for the two particles (i,j) in contact.

The contact tangential force in a specific instant of time, $\mathbf{F}_i^t$, was composed of the elastic spring component, $(\mathbf{F}_i^t)_S$, and the damping component, $(\mathbf{F}_i^t)_D$ (Eq. 10). The elastic constant, S^t, and damping constant, C^t, can be calculated with Eqs. 11 and 12, where $\delta_t \mathbf{n}_i$ is the tangential overlap, $\mathbf{V}_i^t$ is the tangential relative velocity and G^* (Eq. 13) is the equivalent shear modulus related to the shear modulus, G, of particles (i, j).

$$\mathbf{F}_i{}^t = (\mathbf{F}_i{}^t)_S + (\mathbf{F}_i{}^t)_D = S^t \delta_t + C^t (\mathbf{V}_i{}^t) \tag{10}$$

$$S^t = 8G^* \sqrt{R^* \delta_t \mathbf{n}_i} \tag{11}$$

$$C^t = -2\sqrt{\frac{5}{6}} \beta \sqrt{m^* S^t} \tag{12}$$

$$G^* = \frac{G_i G_j}{G_i(1-\nu_j^2) + G_j(1-\nu_i^2)} \tag{13}$$

The 3D silo container was filled with pinewood particles at a constant rate of 4 kg/s. A virtual cubic box of edge 30 cm was used as a random particle generator to reproduce the central filling method used in the experimental tests. The generated particles were allowed to fall under gravity from the virtual container into the silo, to freely reach a static resting position within it.

The filling process took approximately 24 s, followed by allowing the deposit to relax until the total kinetic energy of the particles felt below 10^{-8} J. Afterward, discharge began by removing the outlet. A time step of $5 \cdot 10^{-6}$ s was used in the simulations, which is 7.5% of the Rayleigh time step [28]. This ensured the robustness of the calculations and helped avoid significant fluctuations in the results for subsequent steps. A partial discharge of the silo (with a total discharge time of 22 s) was carried out due to limitations in computer resources.

Simulations were conducted with 250, 000 particles created using the multisphere technique [15] and featuring a polydisperse particle distribution, based on the samples analyzed [18]. Pinewood pellets have a cylindrical shape, with a constant diameter and different lengths.

The sample was divided into five different batches, and each one was reproduced by employing 3 to 8 overlapping individual spheres. The individual spheres used were partially overlapped between 10% and 15% to reach the desired

lengths of the pellets and to approximately match the shape of the particles to cylinders (Fig. 2).

The mean and standard deviation (SD) for the different microscopic properties of the pinewood pellets required for the simulations and the percentage of each of the five types of particles were established from measurements on a sample of 100 randomly selected real pellets (Table 1).

The input parameters required by DEM simulations were determined by the authors [18, 42, 46] employing the required tests, for both particle properties and bulk materials. ISO standards were employed to determine the mechanical properties for bulk materials [29–35]. The input parameters applied in this project, including those experimentally measured, are presented in Table 2. The mean geometrical properties of the pinewood pellets tested are: L_{50} = 15.92 mm, Φ_{50} = 6.01 mm, V_{50} = 450.1 mm^3 and d_{50} = 9.5 mm, where d_{50} is the diameter of the equivalent sphere having the mean volume, V_{50}, of the applied pinewood pellets.

2.3 Model development and validation

The determination of particle properties implies a certain degree of uncertainty because of the procedures performed and the intrinsic heterogeneity of the granular materials. The flow of granular materials through an outlet orifice is a more steady-state process. Thus, the main particle parameters that affect these simulations are those related to friction [9, 61].

Because of that, several DEM models were generated by varying the coefficient of static and rolling friction with regard to pinewood pellets within the confidence interval obtained by Gallego et al. [19]. Five experimental tests with a reduced amount of pinewood pellets (total mass 30 kg) were performed to obtain flow parameters to compare with DEM results to validate the numerical model. In addition, the dimensions of the corrugated steel sheet used in the experimental setup were also adopted for the numerical model (wavelength $l = 0.075$ m, depth of corrugation $h_c = 0.013$ m).

Table 3 shows the comparison between the DEM model developed with the finally adopted parameters (Table 2) and the experimental tests. It can be seen that there is very good agreement for all parameters between both sets of results. The differences are lower than 4% in all cases. The void ratio was also obtained for the numerical model and the experimental tests, and the value is close to 0.6 in both cases, with a small difference of 4.9% between them.

The cumulative discharge mass was also obtained for the experimental and DEM model (Fig. 3), and a very good agreement was again obtained between both sets of results.

The use of non-spherical particles can lead to changes in the results obtained with a numerical simulation [42] for different repetitions. Because of that, a preliminary study was conducted with the DEM model corresponding to the characteristics of the corrugated profile of the experimental setup (wavelength $l = 0.075$ m, depth of corrugation $h_c = 0.013$ m) and 5 repetitions were performed. The numerical results corresponding to the normal and frictional forces obtained on both opposite corrugated walls at relative height $H/d_{50} = 26$ (Fig. 4), as well as the effective wall friction coefficient (Fig. 5), have been obtained during discharge to justify a high repeatability of the simulations.

Figure 4 shows there are no significant differences between the numerical forces obtained at both walls at relative height $H/d_{50} = 26$, whose mean values are approximately 9.2 and 6.25 N for normal and frictional forces, respectively. In addition, the mean standard deviation obtained in all cases is less than 0.17 N, leading to very low coefficients of variation ($< 3\%$ in all cases).

Figure 5 shows that the effective wall friction coefficient slightly decreases during the discharge process. Again, there are no differences between both walls at relative height $H/d_{50} = 26$ and the coefficients of variation obtained are now even lower ($< 1.5\%$ in all cases). These results enable resource optimization through the execution of a single simulation for each numerical model (see Table 4).

3 Results and discussion

Several simulations were carried out considering different values for the basic parameters that define the corrugated wall (Table 4). The geometry used in the study was specifically designed to reflect real-world conditions, with the choice of corrugation wavelength and depth based on existing commercial sinusoidal steel sheet profiles. These dimensions were selected to explore the behavior of the flow under conditions representative of practical applications. All dimensions were normalized with respect to the mean equivalent diameter of the particles tested (d_{50} = 9.5 mm).

3.1 Mass flow rate

It is well known that the mass flow rate (Q) depends mainly on the size ratio between the outlet orifice and the granular material [3]. Figure 6 shows the evolution of the mass flow rate over time during the first 20 s of discharge for each relative depth of corrugation (h_c/d_{50}). The results refer to the mean values obtained for most part of the discharge process, where Q is approximately constant.

The results plotted for every corrugation depth consider all the different wavelengths adopted in simulations and were averaged every $2s$ to avoid intrinsic large fluctuations. The shadowed area corresponds to the standard deviation of the values obtained.

It can be observed that mass flow rate oscillates between 0.58 and 0.68 kg/s during the discharge, and no significant

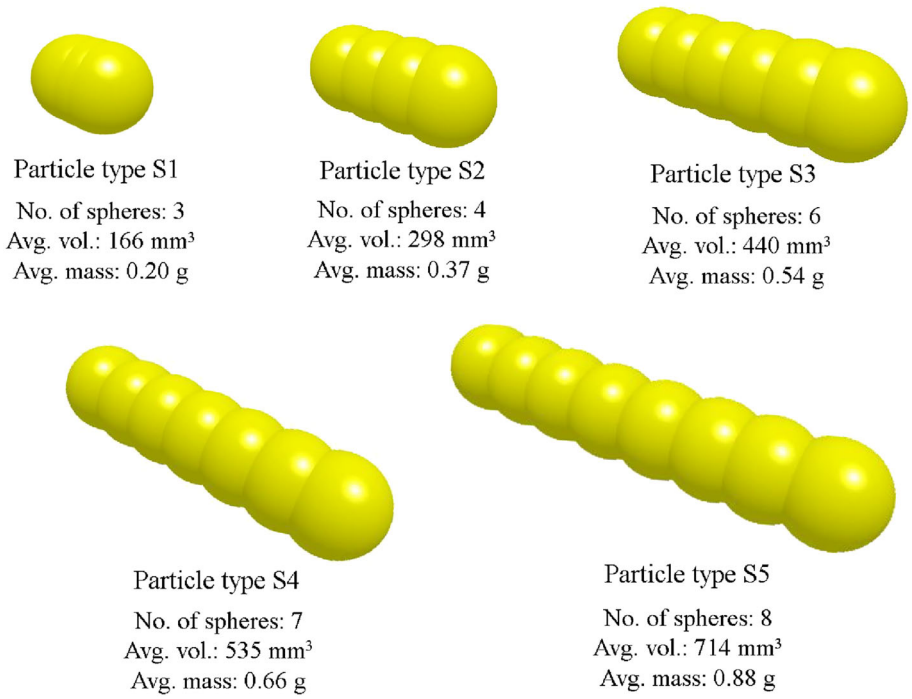

Fig. 2 Particles used in DEM simulations

Table 1 Characteristics of polydispersed particle distribution

Batch sample	Properties			Cap factors for L_p	
	$L_p{}^a$ (mm)	σ^b (mm)	Frequency (%)	Minimum	Maximum
S1	7.86	2.12	14.3	0.80	1.30
S2	12.85	1.46	40.8	0.86	1.16
S3	18.23	1.69	28.6	0.90	1.13
S4	23.67	1.51	12.2	0.95	1.13
S5	29.67	1.53	4.1	0.95	1.05

[a] L_p: mean length; [b] σ: standard deviation

differences appear between the different cases considered for most of the discharge phase. However, the simulations performed with the lowest corrugation depth ($h_c/d_{50} = 1.35$) seem to give a slightly lower mass flow rate than the other models. Because of that, the box plots were created (Fig. 7) for each corrugation depth (h_c/d_{50}) and various relative wavelengths (l/d_{50}) to examine possible differences between Q values.

The results displayed in Fig. 7 show the mean value reported during the discharge process simulated and the fluctuation of the mass flow rate for each numerical case analyzed.

Box-plot results show that the lowest mass flow corresponds with the smooth wall ($h_c/d_{50} = 0$), with an average value of 0.57 kg/s. The results displayed in Fig. 7 show that there is a small positive effect of corrugation on the mass flow rate for all corrugation depths, if the results are compared with the smooth wall ($l/d_{50} = 0$). Mean mass flow rate oscillates in the interval $0.6 - 0.68$ kg/s. However, no statistically significant differences can be found between the different models with corrugated walls, which can be explained because the mass flow rate is mainly governed by the size of the outlet, the particle shape and size [24, 53].

3.2 Shear bands

3.2.1 Particle velocity profile

To define the shear band, the average speed of the particles in the bulk as a threshold ($\overline{v} = 4.5$ mm/s) has been selected. In this way, particles that exceed this barrier will be considered fluidized, while those below it will be considered at rest. Figure 8 shows the velocity field of all particles during discharge in the middle cross section of the silo model at a discharge time T = 10 s for all DEM simulations performed.

The particles flow clearly in the central section of the silo, with velocities larger than $\overline{v}$, while the particles close to the

Table 2 Input parameters applied in DEM simulations

Type	Parameter	Unit	Value
Pinewood pellets	Density, ρ_p	kg/m^3	1227
	Modulus of elasticity, E	N/mm^2	73.34
	Poisson's coefficient, ν		0.40
Steel walls	Density, ρ_p	kg/m^3	7860
	Modulus of elasticity, E	N/mm^2	$2.1 \cdot 10^5$
	Poisson's coefficient, ν		0.30
Methacrylate walls	Density, ρ_p	kg/m^3	1900
	Modulus of elasticity, E	N/mm^2	3149
	Poisson's coefficient, ν		0.45
Particle–particle	Coefficient of restitution, e_{pp}		0.62
	Coefficient of static friction, μ_{sp}		0.40
	Coefficient of rolling friction, μ_{rp}		0.02
Particle–steel wall	Coefficient of restitution, e_{pw}		0.5
	Coefficient of static friction, μ_{sw}		0.3
	Coefficient of rolling friction, μ_{rw}		0.01
Particle–methacrylate wall	Coefficient of restitution e_{pw}		0.67
	Coefficient of static friction, μ_{sw}		0.4
	Coefficient of rolling friction, μ_{rw}		0.01

Table 3 Experimental parameters measured for DEM validation

Variable	DEM	Experimental tests			Difference
	Model	Mean	σ	CV(%)	(%)
Discharge time, T (s)	23	22.67	2.08	9.18	1.46
Mass discharged, M (kg)	11.57	11.15	1.04	9.33	3.77
Mass flow rate, Q (kg/s)	0.63	0.62	0.03	5.06	1.61
Angle of repose, ϕ_r	40.90	40.54	1.23	3.04	0.89
Void ratio, e	0.587	0.618	0.008	1.3	4.9

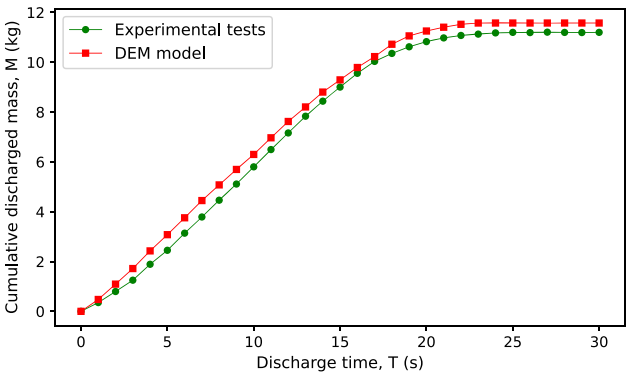

Fig. 3 Comparison of experimental and DEM results for cumulative discharged mass

corrugated walls are mainly at rest (with velocities significantly lower than the threshold value).

The width of the material at rest is greater for those locations closer to the bottom of the silo (blue color in Fig. 8) in all simulations.

In addition, the inclination of the shear band with respect to the horizontal pressure is in the interval $\alpha = 68 - 75°$. Wolf et al. [55] confirmed that the orientation of a shear band against the direction of minor compressive stress according to the Coulomb theory [11] would be $(\pi/4 + \phi/2)$, where ϕ is the angle of internal friction of the material. The angle of internal friction of the pinewood pellets obtained by the authors was $\phi = 40.7°$ [46]; thus, the inclination of the reported shear band is very close to the value proposed by Mohr–Coulomb for an active stress state.

3.2.2 Particle velocity at different heights

In order to examine the influence of the corrugation depth and wavelength on particle velocity, the vertical component of velocity was determined at four silo heights (Fig. 9), measured from silo bottom, and four vertical lines (Fig. 10) at discharge time T= 5 s. The values of lateral components of particle velocities are negligible, and thus, they were not considered. The dimensions (width x height x length) of the

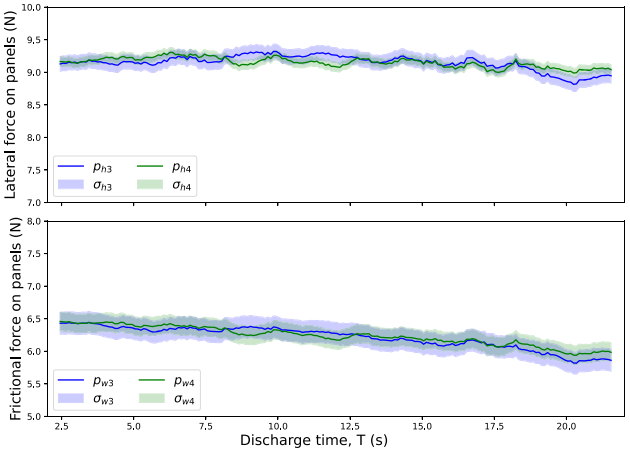

Fig. 4 Normal (p_h) and tangential numerical forces (p_w) obtained at relative height ($H/d_{50} = 26$), and the corresponding standard deviations (σ_h and σ_w) during the discharge process

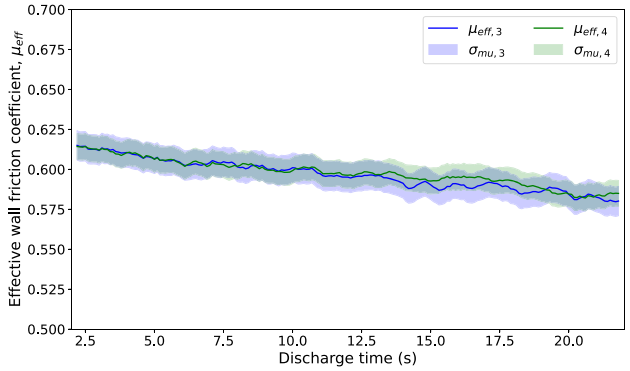

Fig. 5 Numerical effective wall friction coefficient (μ_{eff}) obtained at relative height ($H/d_{50} = 26$), and the corresponding standard deviations (σ_{mu}) during the discharge process

Representative Volume Element (RVE) were $4.2d_{50}$ x $7.9d_{50}$ x $10.5d_{50}$ and $3.2d_{50}$ x $3.2d_{50}$ x $10.5d_{50}$, for horizontal and vertical lines.

Figure 9 shows that maximum particle velocity appears at the center of the silo outlet, which is in agreement with the findings of previous works conducted by several researchers [8, 19]. The particle velocity decreases when approaching the corrugated walls because the material is at rest on the wall.

Particle velocities increase as the relative height (defined as H/d_{50}) approaches the outlet, where the material is freely flowing. During silo discharge, particles are propelled by the driving force, which is the sum of the gravitational force and the resultant contact force exerted on each particle by all its contacting neighbors. The driving force increases rapidly as the particles approach the orifice. Consequently, the acceleration of the particles exceeds the acceleration due to gravity at the orifice level and then decreases rapidly with increasing distance from the orifice.

Table 4 Corrugation depths (h_c) and wavelengths (l) of corrugated walls used in DEM simulations

Corrugation depth		Corrugation wavelength	
h_c (mm)	h_c/d_{50}	l (mm)	l/d_{50}
0	0	50	5.3
13	1.35	75	7.9
26	2.7	100	10.5
39	4.1	125	13.1

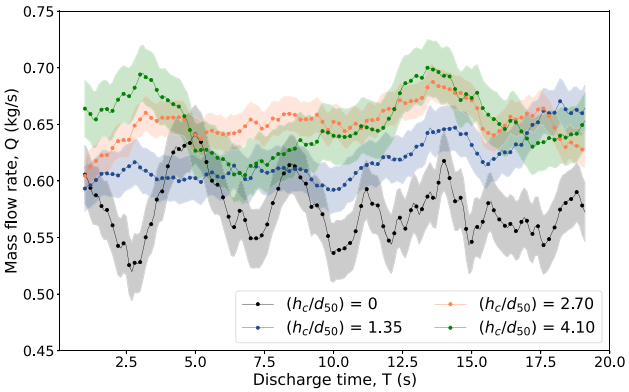

Fig. 6 Evolution of the mass flow rate over discharge time for various relative corrugation depths (h_c/d_{50})

The geometry of the corrugations appears to influence the velocity of the particles, but only to a certain extent. No evident effect of the corrugation depth on the particle mean velocity has been observed for relative wavelength of l/d_{50} greater than 7.9. At a relative height $H/d_{50} = 0$ only for $l/d_{50} = 5.3$, the mean particle velocity increases nonlinearly with increasing corrugation depths.

As the corrugation depth increases, the surface area available for interaction between the particles and the walls also increases, which can lead to greater mobilization of frictional forces and a narrowing of the flame-like region of particles with increased velocity (Fig. 9). These forces help propel the particles more effectively toward the outlet. These results corroborate the findings reported by Gallego et al. [19], who observed no effect of the depth of trapezoidal corrugations with a relative wavelength of 14 in the area close to the discharge orifice.

In the higher parts of the silo, the v value increases only when the corrugation depth increases from 1.35 to 2.7. For example, Fig. 9 shows the mean particle velocity increases at a relative height $H/d_{50} = 4.4$ from 88.2 mm/s ($h_c/d_{50} = 1.35$) to 132.6 mm/s ($h_c/d_{50} = 2.7$). This general trend is observed for all relative heights and corrugation wavelengths, and it is consistent with the findings of Grabowski et al. [23], who also noted that increased wall roughness led to a greater difference in particle displacements near the walls compared to those at the center of the silo.

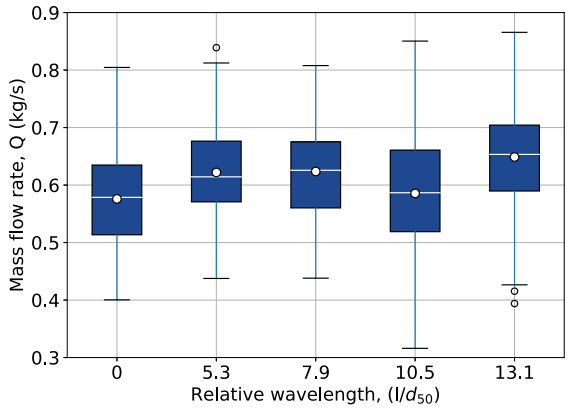

(a) $(h_c/d_{50}) = 1.35$

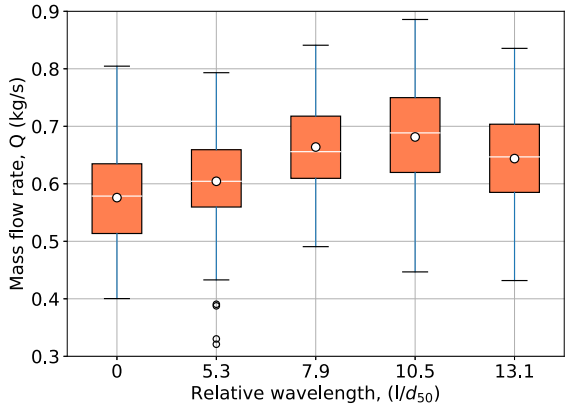

(b) $(h_c/d_{50}) = 2.70$

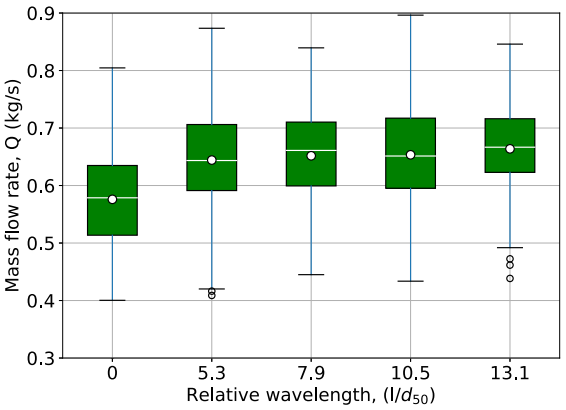

(c) $(h_c/d_{50}) = 4.10$

Fig. 7 Box-plot of DEM simulations for different corrugation depths (h_c/d_{50}) and wavelengths (l/d_{50})

These results suggest the existence of a certain threshold value for the corrugation wavelength, below which an increase in the corrugation depth leads to an increase in particle mean velocity. This threshold value is not constant and is likely determined by the shape and size of the particles. A more in-depth analysis in this field is required, although it is not the objective of this work.

3.2.3 Change of particle velocity with respect to the wall

The location of the shear band is examined through pellet beddings, and it was determined on the basis of the mean particle velocities calculated in four vertical lines of the silo wall, at discharge time T = 5 s (Fig. 10). Regardless of the depth or wavelength of corrugation considered, the particles tend to rest at the locations closest to the silo wall ($x/d_{50} = 2.1$).

Some movement is observed only in a region near the outlet ($H/d_{50} = 10$), where the mean particle velocities are below 2 mm/s, except for the corrugation wavelength $l/d_{50} = 13.1$, where the mean particle velocity is close to 4.5 mm/s.

The particles start the mobilization process at a distance from the wall of ($x_w/d_{50} = 6.3$), and the process is nearly finished at a distance ($x_w/d_{50} = 14.7$) where the particle velocities exceed the threshold value ($\overline{v} = 4.5$ mm/s) for most of the height of the silo. The particle velocities have also been found to tend to increase as the depth of corrugation increases.

Figure 10 shows that at relative distance $x_w/d_{50} = 6.3$ and corrugation wavelength $l/d_{50} = 13.1$ the maximum particle velocity increases from $4.1mm/s$ at $h_c/d_{50} = 1.35$ to $5.3mm/s$ at $h_c/d_{50} = 2.7$, but no change in particle velocity is found for a corrugation depth of $h_c/d_{50} = 4.1$ (v = $5.1mm/s$). In all these cases, the maximum velocities are located at a vertical distance from the outlet $H/d_{50} = 10 - 16$.

The influence of the corrugation wavelength on particle velocity becomes apparent only when the entire material is mobilized, which is observable at ($x_w/d_{50} = 14.7$). The results shown in Fig. 10 do not allow obtaining any significant tendency on the effect of corrugation wavelength. Only it can be observed that the curves corresponding to the smooth wall and the largest wavelength tend to be closer and exhibit the largest particle velocities at this distance to the silo wall.

If the corrugation wavelength would be large enough, then its shape would tend to be similar to that of the smooth wall, thus explaining the similar velocity profiles found for corrugation depths greater than $h_c/d_{50} > 1.35$. The existence of the funnel flow shown in Fig. 8 makes difficult to detect any clear trend in the results.

The velocity of the particles is represented with respect to the distance from the corrugated wall to observe velocity differences and determine the width of the shear band (Fig. 11). Particle velocities are only represented at a maximum distance to the silo wall $x_w/h_c = 14.7$ because the bulk material is fully mobilized in the silo center, and the

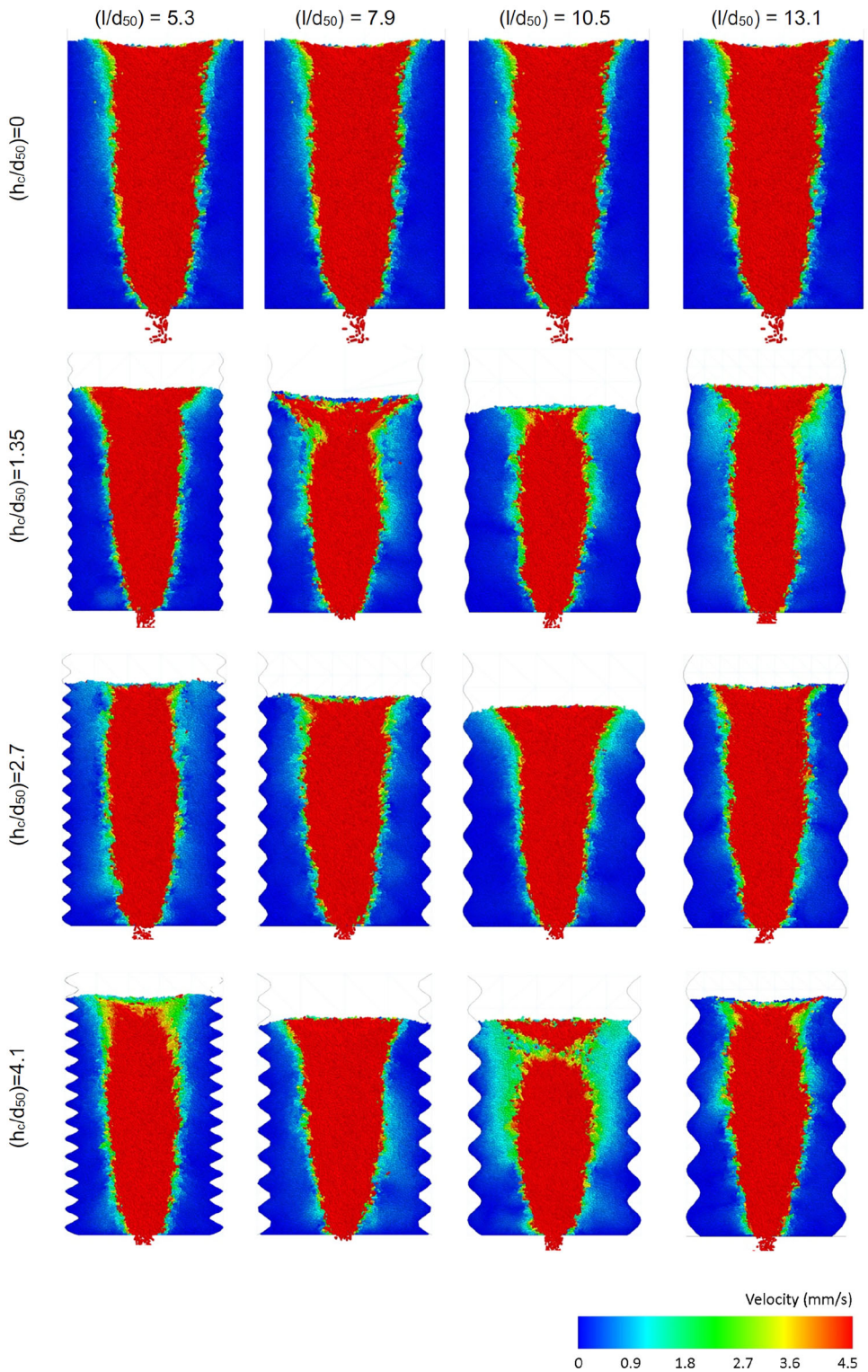

Fig. 8 Particle velocity profiles at a silo cross section for various relative corrugation depths, (h_c/d_{50}), and wavelengths, (l/d_{50})

purpose of this figure was detecting the location and width of the shear band.

The beginning of the shear band is located where the particles velocity exceeds the threshold value ($\overline{v} = 4.5$ mm/s) and is placed approximately at a relative distance $(x_w/d_{50}) = 7.5 - 10$ to the wall for all considered corrugation depths. This means that the beginning of the shear band is located approximately at a distance from 2 to 5 times the mean equivalent diameter of tested particles (d_{50}) from the vertical line connecting the corrugation peak, which is

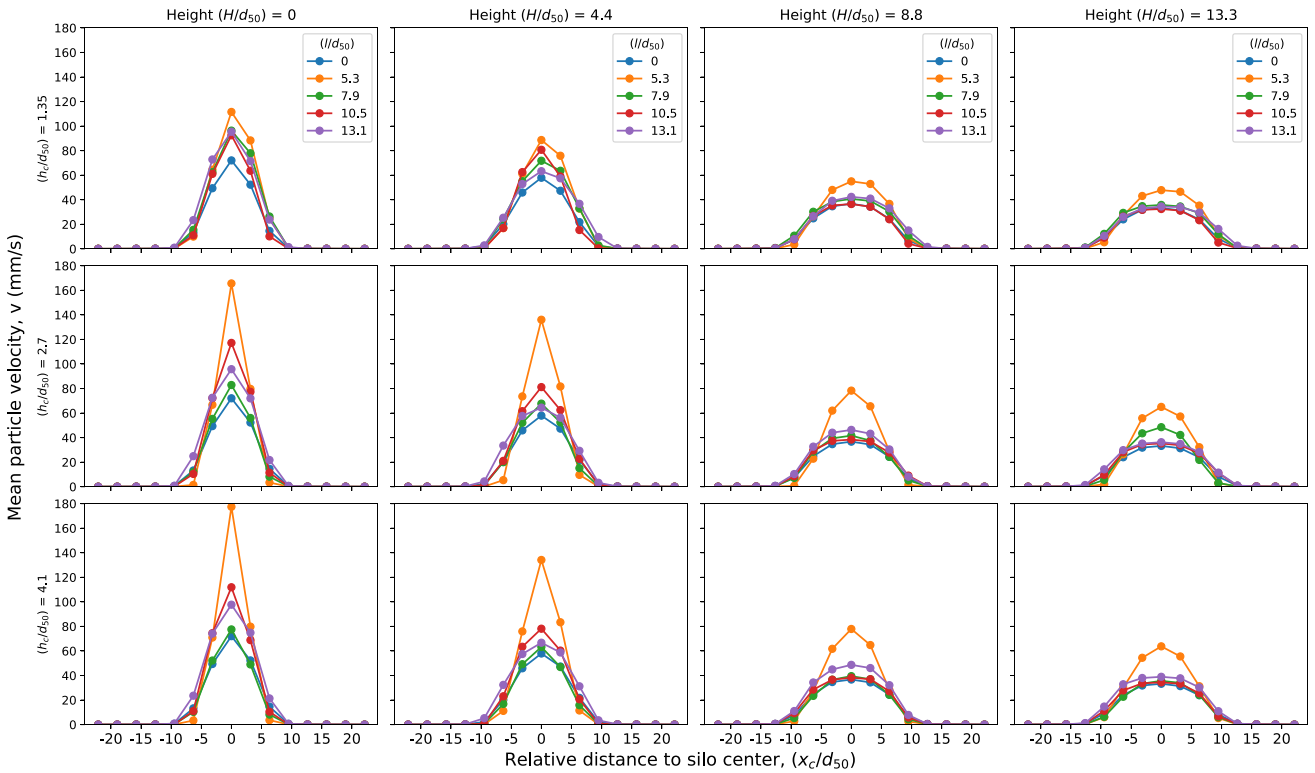

Fig. 9 Particle velocity, v (mm/s), obtained at four silo heights (H/d_{50}) in the central silo cross section, and as a function of the relative corrugation depth, (h_c/d_{50}), and wavelength, (l/d_{50})

consistent with the findings by Gallego et al. [19]. This location slightly varies with silo height, and it is observed to be closer to the corrugations for relative heights greater than $H/d_{50} = 30$.

Figure 11 also shows the beginning of the shear band approaches to the silo wall when increasing the height above the outlet. Besides, those models with a corrugated profile closer to the smooth wall ($l/d_{50} = 0$ and 13.1) show the sharpest increase of the particle velocity. Additionally, particles are fully mobilized at distances from wall greater than $(x_w/d_{50}) = 9 - 12.5$; thus, the width of shear band would be in the interval $3 - 5d_{50}$, a value consistent to those reported by other researchers [39, 47, 55].

3.2.4 Distribution of shear stresses

The shear stress from the "quasi-static" stress tensor [19] was obtained from RVE to verify the location of the shear band.

The distribution of existing shear stresses (τ) within the bulk material was determined at four vertical lines (Fig. 12) and four horizontal bands (Fig. 13), whose RVE dimensions (width x height x length) were $4.2d_{50}$ x $7.9d_{50}$ x $10.5d_{50}$ and $3.2d_{50}$ x $3.2d_{50}$ x $10.5d_{50}$, respectively. Figure 12 shows that the shear stress increases with increasing depths of the granular material, which is in agreement with the rate of change of frictional wall stresses proposed in EN 1991-4. It can be also observed that the shear stress also increases from the corrugated wall up to a relative distance $(x_w/d_{50}) = 10.5$ for all examined corrugation depths and wavelengths. Beyond this point, there is no further increase in bulk shear stress, and a decrease is even reported.

The maximum shear stresses obtained are close to 5 kPa and a decrease in τ value with increasing corrugation depths is observed. For example, the DEM model with $(l/d_{50}) = 10.5$ predicts a maximum shear stress $\tau = 5.41$ kPa at a relative wall distance of $(x_w/d_{50}) = 10.5$ for a corrugation depth of $(h_c/d_{50}) = 1.35$, which decreases to a shear stress of $\tau = 4.49$ kPa for a corrugation depth of $(h_c/d_{50}) = 4.1$.

This trend is observed for all wavelengths. However, it vanishes for the relative distances from silo wall higher than $(x_w/d_{50}) = 10.5$. The highest τ values were obtained for the largest corrugation wavelength, but the effect of this parameter was more profound and pronounced near the silo wall. Although no effect of the corrugation geometry on the particle velocities in these areas of the bedding has been observed (see Fig. 12), a strong impact on the shear stress was found, indicating another factors determining the shear stress at the contact point. The most evident differences in the shear stress for varying $l/_{d50}$ values can be observed in the lower parts of the silo, where particles flow nearly freely.

Figure 13 shows the horizontal distribution of shear stress at four vertical locations for all numerical models considered. The results obtained corroborate the observations related to the velocity profiles. The maximum shear stresses are

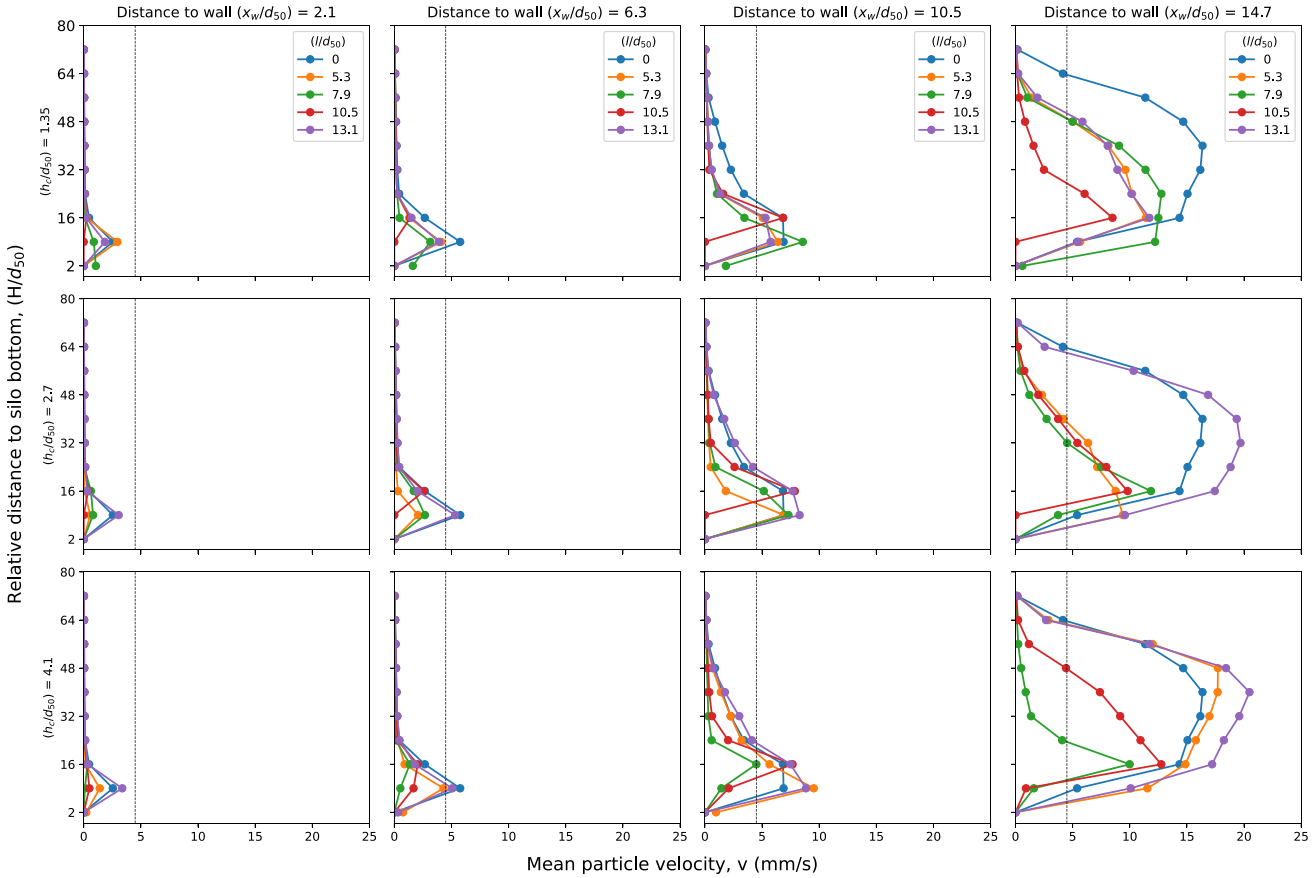

Fig. 10 Mean particle velocity, $\overline{v}$ (mm/s), determined at four vertical lines (x_w/d_{50}) from the corrugated wall in the central silo cross section, and as a function of the relative corrugation depth, (h_c/d_{50}), and wavelength, (l/d_{50})

located at relative distances from the silo wall in the range of $x_w/d_{50} = 5-10.5$. This distance increases with the corrugation depth because the shear band is consistently positioned at a distance $(1-3.5)d_{50}$ from the vertical line connecting the corrugation peaks. Shear stresses tend to be minimal at the central area of the cross section, above the silo outlet.

3.3 Mobilization of wall friction

3.3.1 Wall frictional forces

During the first 20 s of discharge, the relative values of the friction forces (F_w/W) on all walls, defined as a ratio between the total friction forces to the total weight of material, and the weight of the material resting on the bottom of the silo divided by the total weight of the material (F_v/W) were determined and presented in Fig. 14.

It can be observed that there is a redistribution of forces during discharge. It can be seen that frictional forces slightly decrease with discharge time for all cases considered, leading to an increase in the weight of the material placed over the silo bottom. There is a significant influence of the corrugation depth on the friction produced over the silo walls. The silo with smooth walls $(h_c/d_{50} = 0)$ has a relative frictional force of $F_w/W = 0.3$ at the beginning of discharge, which is lower than the maximum value obtained $(F_w/W = 0.54)$ for the largest corrugation depth $(h_c/d_{50} = 4.1)$.

Figure 14 shows that frictional forces increase when the corrugation depth increases for all the corrugation wavelengths considered. For example, (F_w/W) progressively increases from 0.29 $(h_c/d_{50} = 0)$ to 0.47 $(h_c/d_{50} = 4.1)$ if a corrugation wavelength of $l/d_{50} = 10.5$ is considered. This increment is even larger for a corrugation wavelength of $(l/d_{50}) = 13.1$ for which the total relative frictional force increases from 0.29 to 0.52.

However, the wavelength does not seem to clearly affect the frictional force produced over the silo walls, mainly because of the different behavior exhibited by corrugation wavelength $l/d_{50} = 7.9$. In this case, the distribution of forces obtained for the corrugation depths $(h_c/d_{50} = 2.7$ and $4.1)$ is very similar. Wall lateral pressures and frictional pressures were determined at the wall locations corresponding to the instrumented panels 3 and 4 (Fig. 15) at relative height $(H/d_{50}) = 26$.

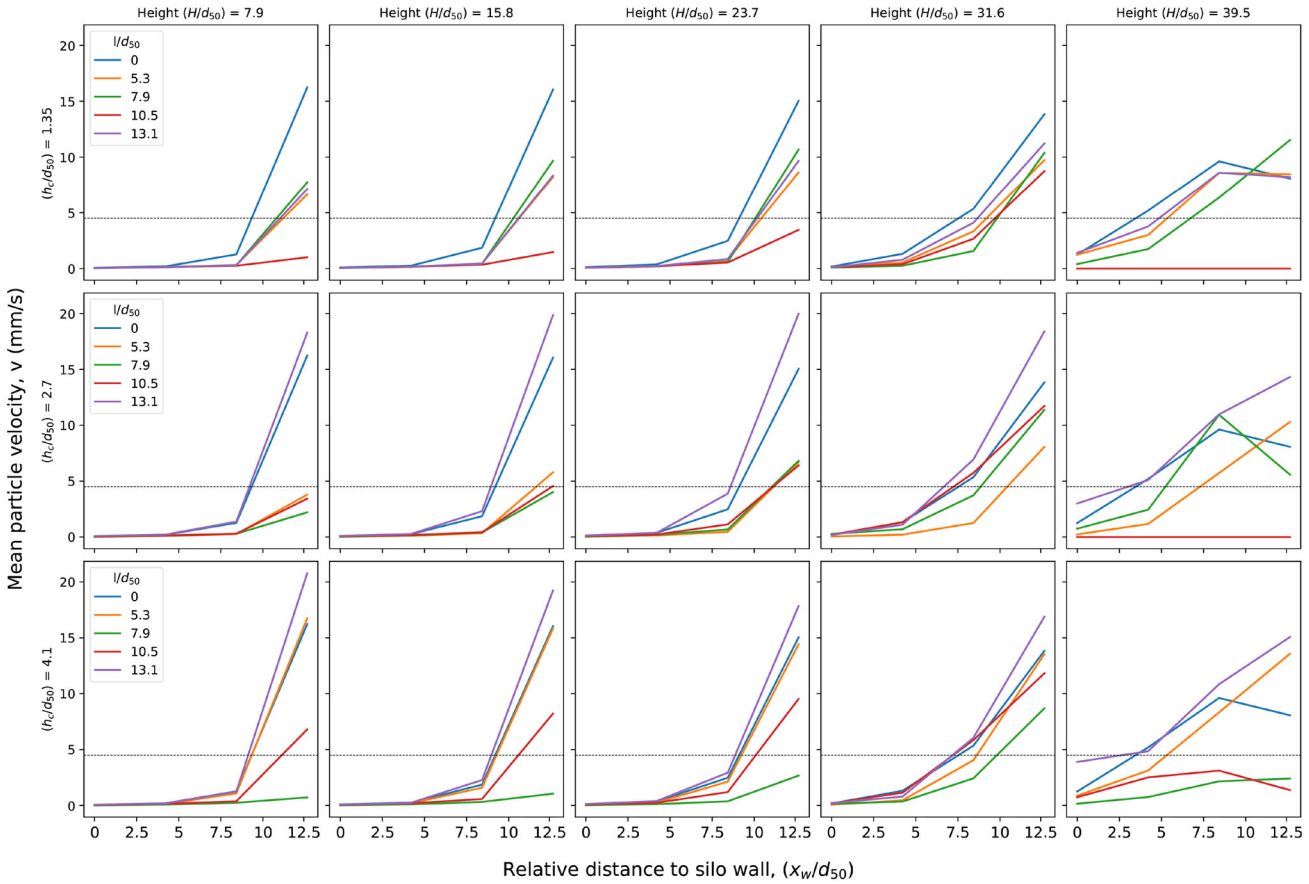

Fig. 11 Mean particle velocity, $\overline{v}$ (mm/s), with respect to relative distance to silo wall (x_w/d_{50}) at five vertical locations (H/d_{50}) in the central silo cross section, and as a function of the relative corrugation depth, (h_c/d_{50}), and wavelength, (l/d_{50})

Figure 15 shows that the wall normal pressure at test panels is always in the range $300-500$ Pa. The lowest lateral pressures are reported for the smallest corrugation wavelength in all cases, except for the corrugation depth $h_c/d_{50} = 4.1$, where the lowest value is reported for a corrugation wavelength $l/d_{50} = 13.1$. In addition, the maximum lateral pressures appear for a corrugation wavelength $l/d_{50} = 7.9$ for all models, and then a reduction in the lateral pressures of the wall is reported for larger wavelengths.

The frictional pressures of the wall are clearly affected by the characteristics of the corrugations. The wall frictional pressure tends to increase with increasing values of the corrugation depth or decreasing wavelengths. For example, wall frictional pressure increases from 124.3 Pa for the smooth wall ($h_c/d_{50} = 0$) up to 501.4 Pa for a corrugation depth of $h_c/d_{50} = 4.1$. However, the results corresponding to $l/d_{50} = 7.9$ show a different behavior.

The influence of the wavelength of corrugations on the frictional pressure has also been found, especially for (l/d_{50}) ranging from 7.9 to 13.1. If the wavelength of the corrugation increases, the frictional pressure in the panels decreases for all depths of corrugation considered. The maximum value of p_w for the silo model with a corrugation depth of ($h_c/d_{50} = 2.7$) is 528.6 Pa when a wavelength of (l/d_{50}) $= 7.9$ is considered, while this value reduces to 205.6 Pa for a wavelength of (l/d_{50}) $= 13.1$. It can be also observed that the difference between the frictional pressures determined for smooth wall and the one with the largest corrugation depth also decreases with increasing wavelength values. This difference is 537.2 Pa for (l/d_{50}) $= 7.9$ and is reduced to 154.8 Pa for (l/d_{50}) $= 13.1$. The results obtained for the corrugation wavelength $l/d_{50} = 7.9$ do not follow this trend, since for all corrugation depths analyzed it provides the largest wall frictional pressures. The results obtained at corrugated walls show that the corrugation wavelength of $l/d_{50} = 7.9$ predicts the highest forces over the wall.

3.3.2 Effective wall friction coefficient

The effective wall friction coefficient for the DEM models was calculated as the ratio between the frictional and lateral pressures (Eq. 14) to examine its sensitivity to the depth and

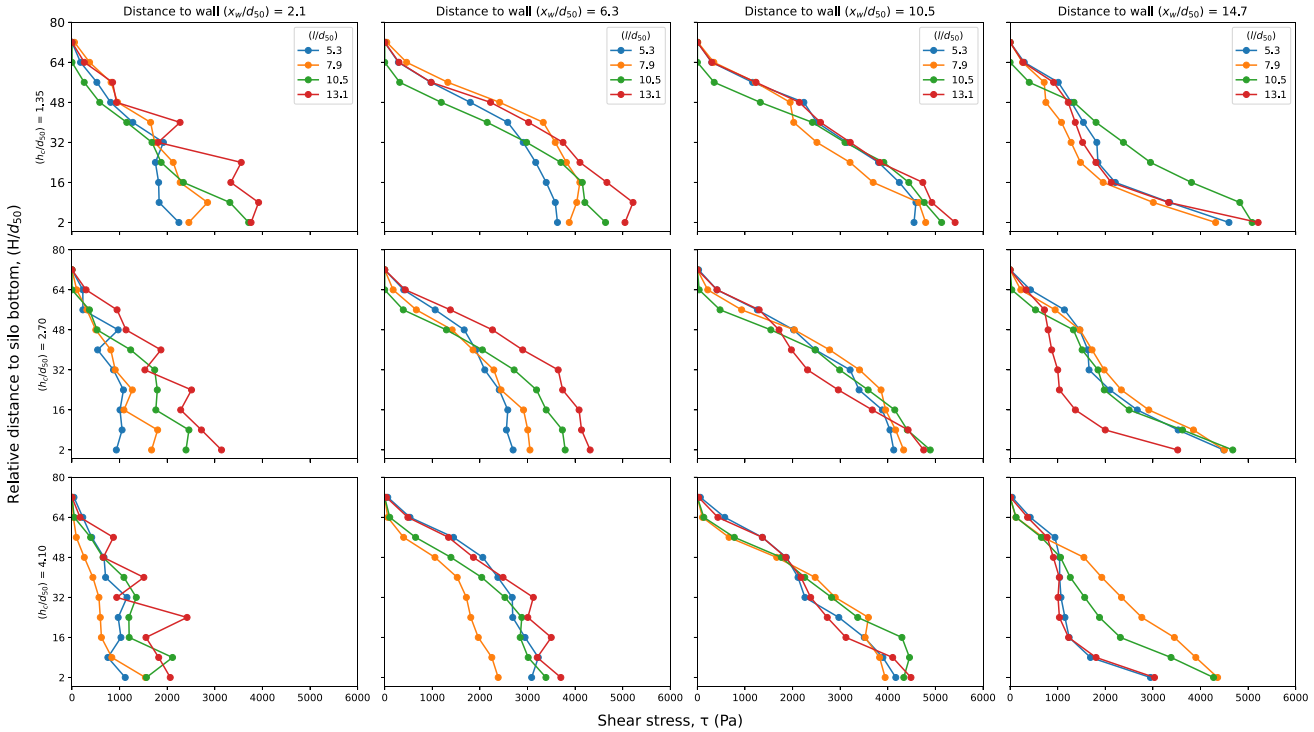

Fig. 12 Change in shear stresses (τ) with respect to relative height (H/d_{50}) at four relative distances from silo wall (x_w/d_{50}) in the central silo cross section for various relative corrugation depths (h_c/d_{50}) and wavelengths (l/d_{50})

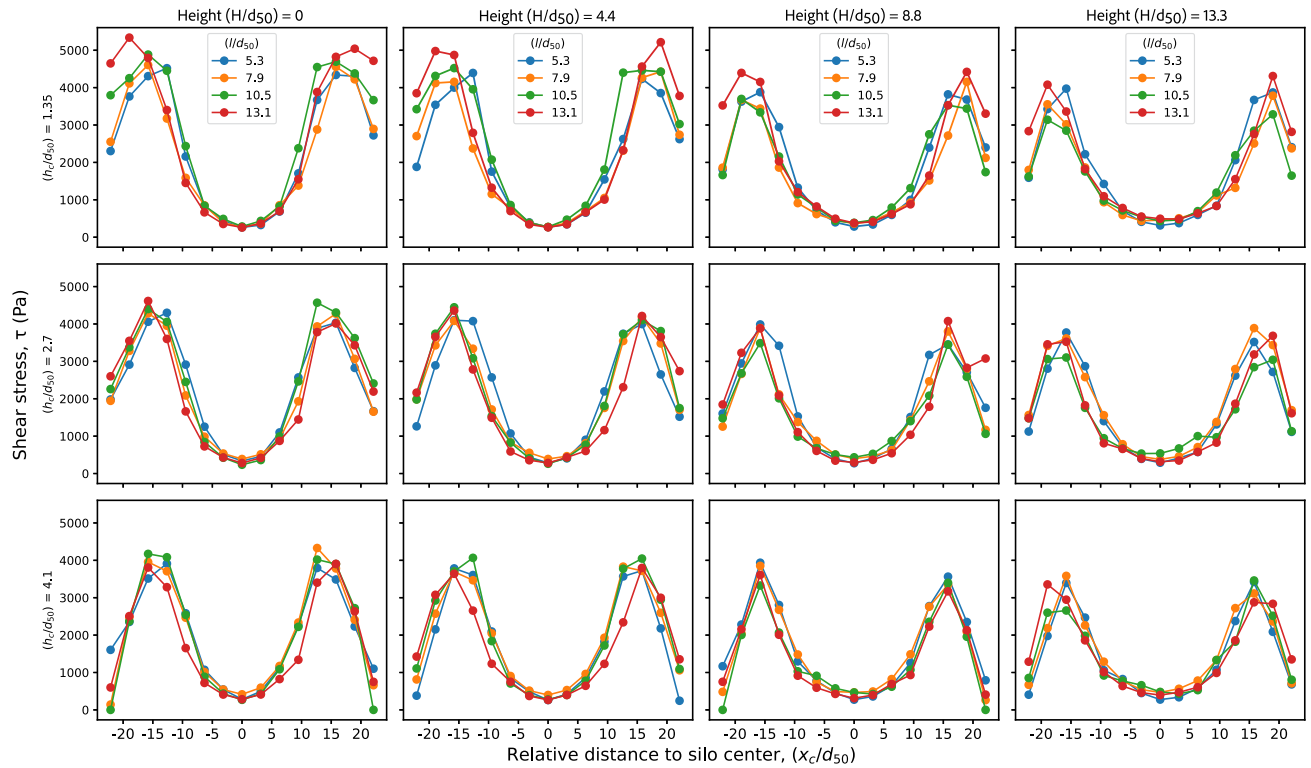

Fig. 13 Change in shear stresses (τ) with respect to relative distances from silo center (x_c/d_{50}) at four relative heights (H/d_{50}) in the central silo cross section for several relative corrugation depths (h_c/d_{50}) and wavelengths (l/d_{50})

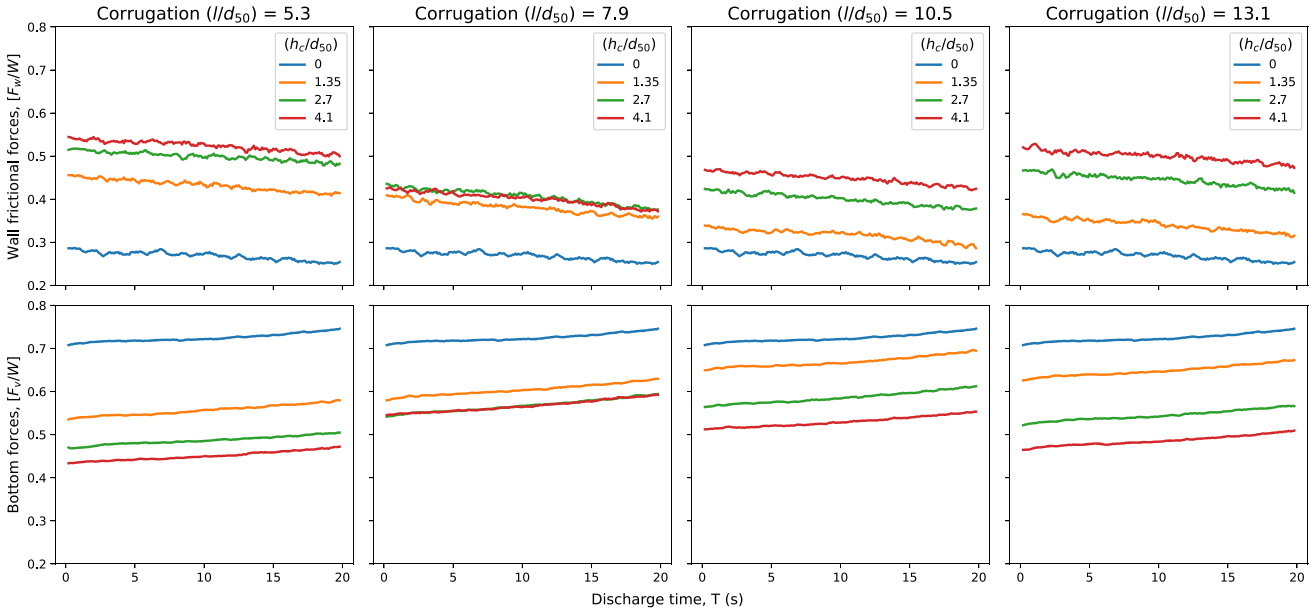

Fig. 14 Evolution of the dimensionless wall frictional forces (F_w/W) and bottom pressures (F_v/W) during discharge time (T) for several relative corrugation depths (h_c/d_{50}) and wavelengths (l/d_{50}), where W is the weight of the stored material

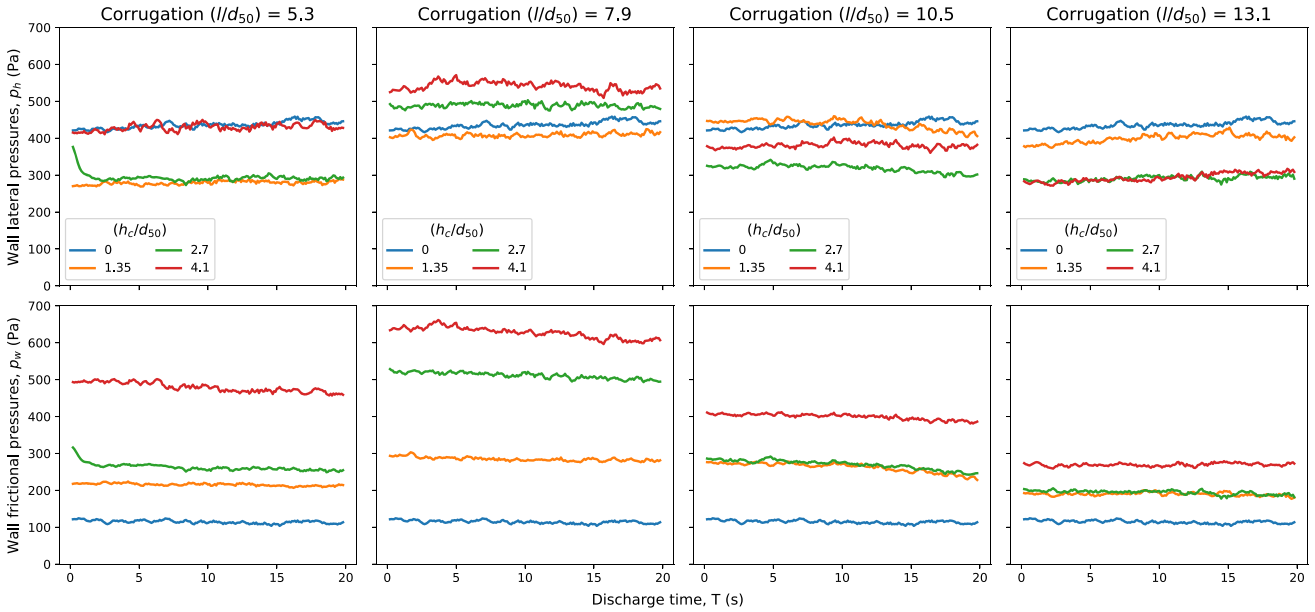

Fig. 15 Wall lateral pressures (p_h) and frictional pressures (p_w) during discharge time (T) as a function of the relative corrugation depth, (h_c/d_{50}), and wavelength, (l/d_{50}), obtained at location of test panels ($H/d_{50} = 26$)

wavelength of corrugations.

$$\mu_{eff,DEM} = p_w/p_h \tag{14}$$

Figure 16 shows the evolution of $\mu_{eff,DEM}$ with the simulation time for both test panels and the smooth silo wall. It can be observed that the effective wall friction coefficient progressively increases during silo filling up to a value of $\mu_{eff,DEM} = 0.27$, which represents 90% of the friction coefficient between pinewood pellets and the steel wall. When the discharge process begins, almost complete friction mobilization occurs and the maximum effective wall friction coefficient equals to $\mu_{eff,DEM} = 0.29$. Next, the effective wall friction coefficient decreases slightly with the discharge time.

The effective wall friction coefficients were also determined for a silo with corrugated walls, matching the geometry of the silo used in the experiments ($h_c/d_{50} = 1.35$

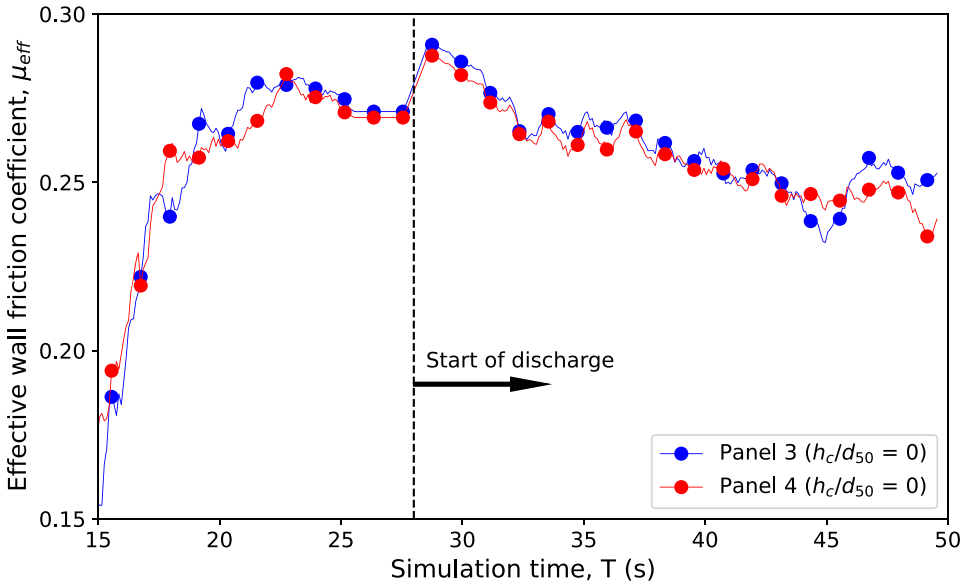

Fig. 16 Evolution of the effective wall friction coefficient ($\mu_{eff,DEM}$) with simulation time (T) for the smooth wall DEM model ($h_c/d_{50} = 0$) at location of test panels ($H/d_{50} = 26$)

and $l/d_{50} = 7.9$). Figure 17 shows the DEM and experimental results obtained at both Panels 3 and 4. Primarily, very good agreement appears between the experimental and numerical results obtained, with differences less than 5% for all cases. Then, it can be observed that $\mu_{eff,DEM}$ reaches a value of 0.66 at the end of filling that increases up to $\mu_{eff,DEM} = 0.72$ during the silo discharge.

According to the theoretical equation proposed by EN 1991-4 for corrugated walls with sinusoidal profiles (Eq. 1), where a wall contact factor $a_w = 0.2$ is proposed for sinusoidal sheet profiles, the effective wall friction coefficient for pinewood pellets should equal to $\mu_{eff,DEM} = 0.78$, when the mechanical parameters obtained for pinewood pellets by the authors (angle of internal friction $\phi = 40.7°$; friction coefficient with the smooth steel wall $\mu_w = 0.3$) are employed. It was found that the experimental (or numerical) values reported are $10 - 15\%$ lower than those proposed by Eurocode EN 1991-4. In addition, EN $1991 - 4$ does not consider variations in μ_{eff} values during filling or discharge phases that have been observed in both experimental tests and numerical simulations. This would imply that the wall contact factors experimentally obtained would be $a_w = 0.35$ and $a_w = 0.25$ for filling and discharge, respectively. These values are greater than the theoretical value suggested by Eurocode for sinusoidal sheet profiles ($a_w = 0.2$).

An effort has been made by the authors to find a relationship between the effective wall friction coefficient and the inertial number [4, 40], but due to a very small rate of change of velocity within the granular system, the dynamics of the bulk material is quasi-static. Thus, the equations used to correlate the inertial number and the wall friction coefficient do not provide coherent results in this system.

Box-plots of the values for the effective wall friction coefficient obtained in numerical simulations during discharge phase were obtained by grouping them according to the corrugation depth and wavelengths (Fig. 18). There is a statistically significant influence of corrugation depth on the effective wall friction coefficient, which is for all cases higher than the coefficient corresponding to a smooth wall ($\mu_{eff,s} = 0.26$).

The value of μ_{eff} increases by about 30% when the corrugation depth increases from 1.35 to 2.70, regardless of the corrugation wavelength. An increase in the corrugation depth from 2.7 to 4.1 results in further increase in μ_{eff} value, although to a lesser extent. A decrease in the effective wall friction coefficient with increasing corrugation wavelength has also observed with percentage increase in μ_{eff} value ranging from 13% to 30% for l/d_{50} values ranging from 5.3 to 13.1.

Grabowski et al.[22] have also reported a relationship between the roughness of the corrugated wall (defined as $R_n = h_c/d_{50}$) and the effective wall friction coefficient. These authors have observed a decrease in the μ_{eff} value with increasing corrugation wavelength, which corroborates the findings of this work. The value of μ_{eff} increased with increasing values of the corrugation depth up to a value ($h_c/d_{50} = 1.0$). No significant changes in μ_{eff} were reported for higher wall roughness. However, these authors examined spherical particles and silo walls with a sawtooth profile, which were significantly different from the cylindrical shape and sinusoidal wall profile adopted in this work.

When the corrugation depth $h_c/d_{50} = 1.35$ is considered, the value of μ_{eff} decreases from 0.65 for $(l/d_{50}) = 5.3$ to 0.42 for $(l/d_{50}) = 13.1$. A decrease in the effective wall friction coefficient with increasing relative corrugation wave-

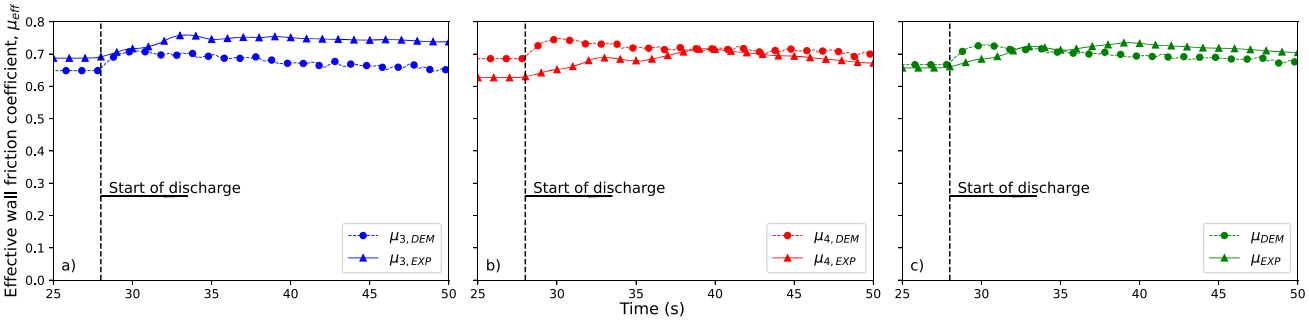

Fig. 17 Numerical (DEM) and experimental (EXP) evolution of the effective wall friction coefficient (μ_{eff}) with time (T) for the corrugated wall with ($h_c/d_{50} = 1.35$) and ($l/d_{50} = 7.9$)), at the height of test panels ($H/d_{50} = 26$) for a) Panel 3 b) Panel 4 c) Average value between panels

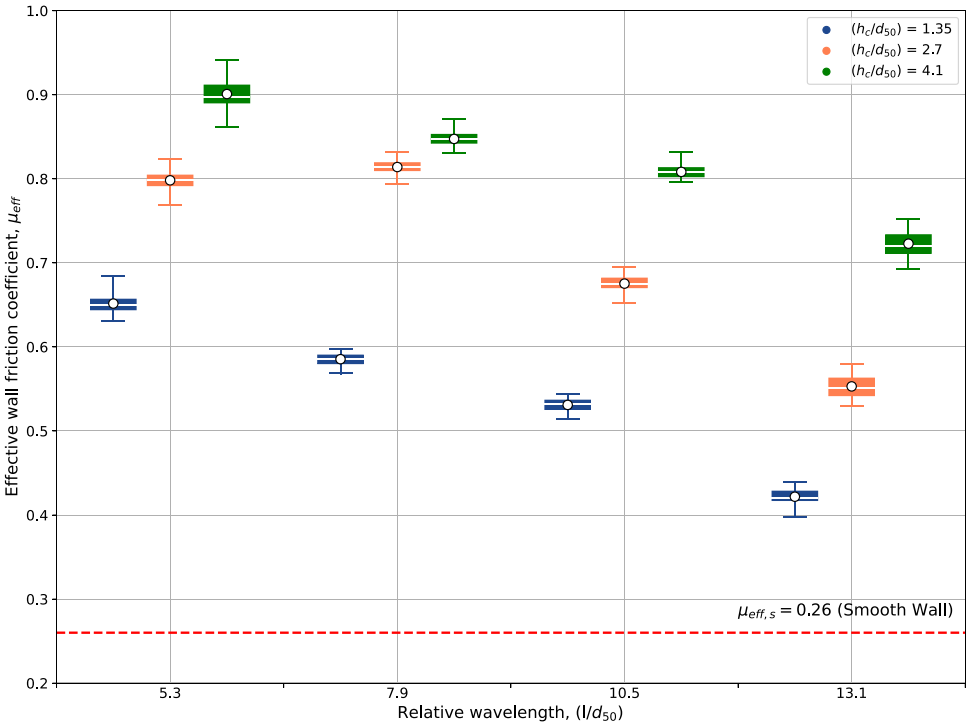

Fig. 18 Box-plots of the effective wall friction coefficient (μ_{eff}) during silo discharge, grouped by the corrugation wavelengths (l/d_{50}) and corrugation depths (h_c/d_{50}) at location of test panels ($H/d_{50} = 26$)

length was observed for all depths of corrugation considered in the DEM models. This trend was related with the particle velocities analyzed in section 3.2. A decrease in the particle velocities with increasing corrugation wavelength results in a decrease in the coefficient of friction that was also observed by Zhang et al. [58].

The DEM results obtained for the numerical models developed by varying the wavelength and depth of wall corrugations show that the effective wall friction coefficient can vary in the range $\mu_{eff} = 0.42 - 0.9$. This finding contradicts the prediction of Eurocode EN 1991-4 that there exists a single value for the equivalent wall friction coefficient ($\mu_{eff,EN} = 0.78$). Therefore, the wall contact factor can also vary between ($a_w = 0.8$) and ($a_w = 0$). If wavelengths are large and corrugation depths are small, then the sinusoidal profile tends to approach a smooth wall. Therefore, the friction against the corrugated wall is mainly governed by the effect of friction against the smooth wall, which means that the wall contact factor would be greater than the value proposed by the standard ($a_w = 0.2$) and the effective wall friction coefficient would be lower than the theoretical one.

On the other case, for large corrugation depths and small wavelengths many particles are trapped inside the corrugation valley, increasing the effect of friction between individual particles. Because of that, the equivalent friction coefficient against the corrugated wall can reach the maximum value, which is equal to tan ϕ_i. The wall contact factor is then zero ($a_w = 0$), reaching a value even lower than the one proposed by EN 1991-4. Figure 18 shows that the maximum effective wall friction coefficient was obtained for the DEM

model with the largest corrugation depth ($h_c/d_{50} = 4.1$) and the smallest wavelength ($l/d_{50} = 5.3$).

4 Conclusions

This research analyzes the effects that a corrugated steel wall can produce on the flow, wall pressures and friction mechanism for non-spherical particles, considering different corrugation depths and wavelengths. A three-dimensional discrete element model of a silo was developed and experimentally validated to assess particle velocities during the discharge process, the relative location of the shear band in relation to the silo wall and the relationship between the effective wall friction coefficient and the geometry of the corrugated sheet. The geometrical parameters of the corrugations were selected to reflect real-world conditions found in the existing commercial silos with sinusoidal steel sheet profiles. The main conclusions derived from the results presented in this paper are as follows:

- There is good agreement between the numerical and experimental discharge flow rates, with differences less than 4% for all considered cases. Although the differences in mass flow rates are not notably remarkable, since the mass flow rate is mainly governed by the outlet size and the shape and size of the particles, the numerical models with lower corrugation depths seem to provide a slightly lower mass flow rate. Similarly, the numerical models with higher corrugation wavelength exhibited slightly higher discharge flow rate as compared to the smaller wavelength.
- Analysis of the velocity fields shows that the geometry of the corrugated sheet affects the velocity of the particles. In the central part of the silo, the velocity of the granular material is higher in models with larger corrugation depths, compared to models with smaller corrugation depths. On the other hand, the velocity of the particles tends to be higher as the corrugation wavelength decreases.
- The beginning of the shear band is located approximately at a distance from the vertical line connecting two consecutive corrugation peaks closest to the silo outlet between 1 and 3.5 times the average size of the particles. The thickness of the band is between 5 and 7.5 times the mean particle size. The granular material is completely mobilized from this distance onwards.
- For all models, the maximum shear stresses are located close to the bottom of the silo, with a tendency to decrease as the depth of the corrugation increases. The horizontal distribution of shear stresses corroborates the observations found with regard to the velocity profiles and the location of the shear band.
- The results of the simulations show that there is a significant influence of the depth of corrugation on the friction produced on the walls of the silo during discharge process, with a significant increase in friction forces as the depth of corrugation increases. The influence of the wavelength of the corrugations on the frictional pressures has also been found, with a decrease in the frictional forces with increasing corrugation wavelength. On the other hand, the numerical results indicate that there is no significant effect of the wavelength or depth of the corrugations on the normal pressures.
- The effective wall friction coefficient based on the DEM simulations agrees well with the one obtained experimentally. In the case of the smooth wall silo, a maximum value of 0.29 was recorded at the beginning of silo discharge, which was very similar to the friction coefficient between the pine wood pellets and the steel wall. Meanwhile, the numerical effective wall friction coefficients vary in the range from 0.42 to 0.9 for various wavelengths and the depths of the corrugation, indicating that there is no single value of $\mu_{eff} = 0.78$ as proposed by Eurocode EN $1991 - 4$. The results show that there is a statistically significant influence of the depth and the wavelength of corrugation on the effective friction coefficient, since in all cases the higher wall friction coefficients were obtained as compared to the one corresponding to the smooth wall. The effective wall friction coefficient exhibits a tendency to increase with increasing corrugation depth, regardless of the wavelength considered. On the other hand, an increase in the corrugation wavelength results in a decrease in the μ_{eff} value.

The results obtained in this work help to understand the friction mechanism that exists in the corrugated walls of silos and to check the validity of the equations proposed in the standards. However, further work should be done to consider other aspects, such as the width of the outlet or the filling method, among other factors. In addition, these findings might contribute to practical applications in the industry, such as a more efficient handling of granular materials, a more accurate prediction of the discharge flow of material in a silo or a more precise knowledge of the pressures exerted against the walls of the corrugated silo to optimize its design and that of the wall stiffeners.

Further DEM simulations would be required to check these findings by using a silo geometry that ensures the existence of a mass flow, or the inclusion of different bottom configurations, such as centric or eccentric hoppers.

Acknowledgements The authors gratefully acknowledge the Spanish "Agencia Estatal de Investigación" for funding this research (grant number PID2019-107051GBI00/AEI/10.13039/501100011033), and the Universidad Politécnica de Madrid (www.upm.es) for providing computing resources on Magerit Supercomputer.

Funding Open Access funding provided thanks to the CRUE-CSIC agreement with Springer Nature.

Data availability All data used during this study are available from the corresponding author by request.

Declarations

Conflict of interest The authors declare that they have no conflict of interest.

References

1. Adesina P, O'Sullivan C, Wang T (2024) DEM study on the effect of particle shape on the shear behaviour of granular materials. Comput Part Mech 11:447–466. https://doi.org/10.1007/s40571-023-00632-8
2. Ayuga F (2008) Some unresolved problems in the design of steel cylindrical silos. In: Structures and Granular Solids: From Scientific Princ. to Eng. Appl. - An Int. Conf. in Celebration of the 60th Birthday of Prof. J. Michael Rotter - Proc. Int. Conf. on Structures and Granular Solids, pp 135–146. https://doi.org/10.1201/9780203884447.ch12
3. Beverloo WA, Leniger HA, de Velde JV (1961) The flow of granular solids through orifices. Chem Eng Sci 15:260–269
4. Boyer F, Guazzelli Élisabeth, Pouliquen O (2011) Unifying suspension and granular rheology. Phys Rev Lett 107:188301. https://doi.org/10.1103/PhysRevLett.107.188301
5. Caitano R, Garcimartín A, Zuriguel I (2023) Anchoring effect of an obstacle in the silo unclogging process. Phys Rev Lett 131:098201. https://doi.org/10.1103/PHYSREVLETT.131.098201
6. CEN: (2006) EN 1991-4. Eurocode 1 - Actions on structures - Part 4: Silos and tanks, 1 edn. CEN
7. Cheikh KE, Rémond S, Pizette P, Vanhove Y, Djelal C (2016) Discrete element study of granular material - bumpy wall interface behavior. Physica A 457:526–539. https://doi.org/10.1016/j.physa.2016.03.053
8. Chung Y, Kuo T, Hsiau S (2022) Effect of various inserts on flow behavior of Fe_2O_3 beads in a three-dimensional silo subjected to cyclic discharge- part I: Exploration of transport properties. Powder Technol 400:117220. https://doi.org/10.1016/j.powtec.2022.117220
9. Coetzee CJ (2017) Review: calibration of the discrete element method. Powder Technol 310:104–142. https://doi.org/10.1016/j.powtec.2017.01.015
10. Combarros M, Feise HJ, Zetzener H, Kwade A (2014) Segregation of particulate solids: experiments and DEM simulations. Particuology 12:25–32. https://doi.org/10.1016/j.partic.2013.04.005
11. Coulomb C (1773) Essai sur l'application des règles des maximis et minimis à quèlques problèmes de statique relatifs à l'architecture. Mémoires de Mathématique et de Physique, Académie Royale des Sci 7:343–382
12. Cundall P, Strack O (1979) A discrete numerical model for granular assemblies. Géotechnique 29(1):47–65. https://doi.org/10.1680/geot.1979.29.1.47
13. Debnath B, Kumaran V, Rao KK (2023) Dense granular flow through a flat-bottomed silo: comparison of the DEM and continuum models with experiments. Powder Technol. https://doi.org/10.1016/j.powtec.2023.119036
14. EDEM (2023) DEM Solutions Ltd User Guide. EDEM
15. Favier JF, Abbaspour-Fard MH, Kremmer M, Raji AO (1999) Shape representation of axi-symmetrical, non-spherical particles in discrete element simulation using multi-element model particles. Eng Comput 16(4):467–480
16. Fuentes JM, Pinilla A, Madrid M, Wiącek J, Ayuga-Téllez E, Ayuga F, Gallego E (2024) Measurement of friction phenomena on silo walls made of corrugated steel. Comput Electron Agric 226:109374. https://doi.org/10.1016/j.compag.2024.109374
17. Gago PA, Madrid MA, Boettcher S, Blumenfeld R, King P (2023) Effect of bevelled silo outlet in the flow rate during discharge. Powder Technol 428:118842. https://doi.org/10.1016/j.powtec.2023.118842
18. Gallego E, Fuentes JM, Ruiz A, Hernández-Rodrigo G, Aguado P, Ayuga F (2020) Determination of mechanical properties for wood pellets used in DEM simulations. Int Agrophys 34:485–494. https://doi.org/10.31545/intagr/130634
19. Gallego E, Fuentes JM, Wiącek J, Villar JR, Ayuga F (2019) DEM analysis of the flow and friction of spherical particles in steel silos with corrugated walls. Powder Technol. https://doi.org/10.1016/j.powtec.2019.07.072
20. Golshan S, Esgandari B, Zarghami R, Blais B, Saleh K (2020) Experimental and DEM studies of velocity profiles and residence time distribution of non-spherical particles in silos. Powder Technol 373:510–521. https://doi.org/10.1016/j.powtec.2020.06.093
21. González-Montellano C, Ramírez A, Gallego E, Ayuga F (2009) On the steel cost of circular flat-bottomed silos designed using the eurocodes. Struct Eng Mech 33:561–572. https://doi.org/10.12989/sem.2009.33.5.561
22. Grabowski A, Nitka M, Tejchman J (2021) 3D DEM simulations of monotonic interface behaviour between cohesionless sand and rigid wall of different roughness. Acta Geotech 16:1001–1026. https://doi.org/10.1007/s11440-020-01085-6
23. Grabowski A, Nitka M, Tejchman J (2021) Micro-modelling of shear localization during quasi-static confined granular flow in silos using DEM. Comput Geotech 134:104108. https://doi.org/10.1016/j.compgeo.2021.104108
24. Gui N, Yang X, Tu J, Jiang S (2017) Effect of roundness on the discharge flow of granular particles. Powder Technol 314:140–147. https://doi.org/10.1016/j.powtec.2016.09.056. (Special Issue on Simulation and Modelling of Particulate Systems)
25. Hatano T (2007) Power-law friction in closely packed granular materials. Phys Rev E 75:060301. https://doi.org/10.1103/PhysRevE.75.060301
26. Horabik J, Parafiniuk P, Molenda M (2018) Stress profile in bulk of seeds in a shallow model silo as influenced by mobilisation of particle-particle and particle-wall friction: Experiments and DEM simulations. Powder Technol 327:320–334. https://doi.org/10.1016/j.powtec.2018.01.003
27. Horabik J, Parafiniuk P, Wiącek J, Kobyłka R, Molenda M, Stasiak M (2022) DEM modelling of the influence of initial stress state on the discharge rate of spherical particles from a model silo. Powder Technol 403:117402. https://doi.org/10.1016/j.powtec.2022.117402

28. Huang YJ, Nydal OJ, Yao B (2014) Time step criterions for nonlinear dense packed granular materials in time-driven method simulations. Powder Technol 253:80–88. https://doi.org/10.1016/j.powtec.2013.10.010
29. ISO (2014) Geotechnical investigation and testing–laboratory testing of soil–part 2: determination of bulk density (ISO 17892-2:2014). International Organization for Standardization
30. ISO (2016) Geotechnical investigation and testing - laboratory testing of soil - part 4: determination of particle size distribution (ISO 17892-4:2016). International Organization for Standardization
31. ISO (2017) Geotechnical investigation and testing–laboratory testing of soil–part 5: incremental loading oedometer test (ISO 17892-5:2017). International Organization for Standardization
32. ISO (2017) Solid biofuels. determination of moisture content. oven dry method–part 2: total moisture. simplified method (ISO 18134-2:2017). International Organization for Standardization
33. ISO (2018) Geotechnical investigation and testing–laboratory testing of soil–part 1: determination of water content (ISO 17892-1:2018)
34. ISO (2018) Geotechnical investigation and testing–laboratory testing of soil–part 10: direct shear tests (ISO 17892-10:2018). International Organization for Standardization
35. ISO (2019) Geotechnical investigation and testing–laboratory testing of soil–part 8: unconsolidated undrained triaxial test (ISO 17892-8:2019). International Organization for Standardization
36. Jop P, Forterre Y, Pouliquen O (2006) A constitutive law for dense granular flows. Nature 441:727–730. https://doi.org/10.1038/nature04801
37. Kobyłka R, Horabik J, Molenda M (2017) Numerical simulation of the dynamic response due to discharge initiation of the grain silo. Int J Solids Struct 106:27–37. https://doi.org/10.1016/j.ijsolstr.2016.12.001
38. Kobyłka R, Molenda M, Horabik J (2020) DEM simulation of the pressure distribution and flow pattern in a model grain silo with an annular segment attached to the wall. Biosys Eng 193:75–89. https://doi.org/10.1016/j.biosystemseng.2020.02.013
39. Lei D, Huang J, Xu W, Wang W, Zhang P (2018) Deformation analysis of shear band in granular materials via a robust plane shear test and numerical simulation. Powder Technol 323:385–392. https://doi.org/10.1016/j.powtec.2017.10.027
40. Liu C, Sun Q, Zhou GGD (2016) Velocity profiles and energy fluctuations in simple shear granular flows. Particuology 27:80–87. https://doi.org/10.1016/j.partic.2015.06.003
41. Luding S (2005) Shear flow modeling of cohesive and frictional fine powder. Powder Technol 158:45–50. https://doi.org/10.1016/j.powtec.2005.04.018
42. Madrid MA, Fuentes JM, Ayuga F, Gallego E (2022) Determination of the angle of repose and coefficient of rolling friction for wood pellets. Agronomy 12:424
43. MiDi G (2004) On dense granular flows. The Eur Phys J E 14:341–365. https://doi.org/10.1140/epje/i2003-10153-0
44. Molenda M, Horabik J, Ross IJ, Montross MD (2002) Friction of wheat: grain-on-grain and on corrugated steel. Trans ASAE 45(2), 415–420. https://doi.org/10.13031/2013.8522
45. Moore DW, White GM, Ross IJ (1984) Friction of wheat on corrugated metal surfaces. Trans ASAE 27:1842–1847
46. Moya M, Sánchez D, Villar-García JR (2022) Values for the mechanical properties of wheat, maize and wood pellets for use in silo load calculations involving numerical methods. Agronomy. https://doi.org/10.3390/agronomy12061261
47. Mühlhaus HB, Vardoulakis I (1987) The thickness of shear bands in granular materials. Géotechnique 37(3):271–283. https://doi.org/10.1680/geot.1987.37.3.271
48. do Nascimento JWB, Neto JPL, Montross MD (2013) Horizontal pressures in cylindrical metal silos and comparison with different international standards. Engenharia Agrícola 33:601–611. https://doi.org/10.1590/S0100-69162013000400002
49. Nitka M, Grabowski A (2021) Shear band evolution phenomena in direct shear test modelled with DEM. Powder Technol 391:369–384. https://doi.org/10.1016/j.powtec.2021.06.025
50. Pinilla A, Fuentes J, Wiącek J, Ayuga F, Gallego E (2023) Friction phenomena in a silo model with corrugated steel walls. In: 2023 ASABE Annual International Meeting, pp 2300160. https://doi.org/10.13031/aim.202300160
51. Soltanbeigi B, Podlozhnyuk A, Papanicolopulos S, Kloss C, Pirker S, Ooi J (2018) DEM study of mechanical characteristics of multi-spherical and superquadric particles at micro and macro scales. Powder Technol 329:288–303. https://doi.org/10.1016/j.powtec.2018.01.082
52. Tsuji Y, Tanaka T, Ishida T (1992) Lagrangian numerical simulation of plug flow of cohesionless particles in a horizontal pipe. Powder Technol 71(3):239–250. https://doi.org/10.1016/0032-5910(92)88030-L
53. Uñac R, Vidales A, Benegas O, Ippolito I (2012) Experimental study of discharge rate fluctuations in a silo with different hopper geometries. Powder Technol 225:214–220. https://doi.org/10.1016/j.powtec.2012.04.013
54. Wiącek J, Gallego E, Parafiniuk P, Kobyłka R, Bacnda M, Horabik J, Molenda M (2021) Experimental analysis of wheat-wall friction and grain flow in a steel silo with corrugated walls. Biosys Eng 209:216–231
55. Wolf H, König D, Triantafyllidis T (2003) Experimental investigation of shear band patterns in granular material. J Struct Geol 25(8):1229–1240. https://doi.org/10.1016/S0191-8141(02)00163-3
56. Wójcik M, Sondej M, Rejowski K, Tejchman J (2017) Full-scale experiments on wheat flow in steel silo composed of corrugated walls and columns. Powder Technol 311:537–555. https://doi.org/10.1016/j.powtec.2017.01.066
57. Zhang Q, Britton MG, Keeper RJ (1994) Interactions between wheat and a corrugated steel surface. Trans ASAE 37 (3):951–956. https://doi.org/10.13031/2013.28164
58. Zhang X, Sun W, Wang W, Liu K (2022) Experimental investigation of granular friction behaviors during reciprocating sliding. Friction 10:732–747. https://doi.org/10.1007/s40544-021-0488-2
59. Zhang Y, Jia F, Zeng Y, Han Y, Xiao Y (2018) DEM study in the critical height of flow mechanism transition in a conical silo. Powder Technol 331:98–106. https://doi.org/10.1016/j.powtec.2018.03.024
60. Zhang Z, Liu Y, Zheng B, Li R, Sun P (2021) Discharge characteristics of binary particles in a rectangular hopper with inclined bottom. Comput Part Mech 8:315–324. https://doi.org/10.1007/s40571-020-00332-7
61. Zhou L, Yu J, Liang L, Wang Y, Yu Y, Yan D, Sun K, Liang P (2021) DEM parameter calibration of maize seeds and the effect of rolling friction. Processes. https://doi.org/10.3390/pr9060914